Journal of Magnetism and Magnetic Materials 322 (2010) 1758–1764

Contents lists available at ScienceDirect

Journal of Magnetism and Magnetic Materials

journal homepage: www.elsevier.com/locate/jmmm

The effects of temperature and frequency on the magnetization switching mode in circular MI sensors

Kwaku Eason [a,*], Kok-Meng Lee [b]

[a] Data Storage Insititute, 5 Engineering Drive I, Singapore 117600, Singapore
[b] The George W. Woodruff School of Mechanical Engineering, Georgia Institute of Technology, Atlanta, GA 30332-0405, USA

ARTICLE INFO

Article history:
Received 20 August 2008
Received in revised form
20 November 2009
Available online 2 February 2010

Keywords:
Magneto-impedance effect
Radial domain walls
Meshless methods
Switching mode
Coupled nonlinear micromagnetics

ABSTRACT

This paper presents results computed using a meshless method in a point collocation formulation to investigate the effects of temperature and frequency on the magnetization switching mode in the circular amorphous magneto-impedance sensor (element). Specifically, the solutions characterizing the MI effect are solved from a set of coupled nonlinear equations consisting of the Maxwell's equations, the Landau–Lifshitz–Gilbert equation, and the thermal diffusion equation. This coupled nonlinear space–time model predicts the formation and propagation of dynamic domain walls in switching and it is shown how they contribute to experimentally observed temperature and frequency effects. Computed results (that agree well with reported experimental data) suggest radial domain walls may play a larger role in the MI effect than originally believed even for the realistic conditions considered here at 1 MHz or more.

1. Introduction

The development of highly sensitive magnetic field detectors in both the past and present has afforded a number of novel technologies such as the bit detections of the magneto-resistive (MR) device embedded within the head of a computer hard-disk drive system, and magnetometry using Superconducting QUantum Interference Devices (SQUID) allowing observations of neural signals from within the body [1]. Within the spectrum of magnetic field sensors, each device has its relative strengths and weaknesses. For example, while SQUIDs are remarkably sensitive, they are inherently limited in their potential applications based on a low temperature requirement to promote its fundamental mechanism, superconductivity.

Alternatively, relatively new devices like magneto-impedance (MI) sensors are also on the horizon of interesting developments given its demonstration of high sensitivity and it has received increasing attention since the early 90s. The MI effect, present in small magnetic structures, can be described as a sensitive realignment (or redistribution) of a periodic magnetization, where the realignment is a result of the introduction of the measured dc field, while a primary ac field (due to the ac current) drives the periodic magnetization. For each realignment or value of the measured field, a detectable voltage change emerges. It has also been reported for some devices that the MI sensor demonstrates good thermal stability [2]. A key distinction of devices like the MI sensor is that it offers an impressive balance of sensitivity (10^{-11} T), flexibility (small and portable), and relatively low costs (compared to SQUIDs).

With few exceptions, the prediction of the MI effect has generally involved solving a decoupled set of harmonic equations reduced from Maxwell's equations describing the electromagnetic field and a micromagnetics equation describing the magnetization. Generally speaking, the assumptions for decoupling require that the magnitude of the measured axial field be very large compared to the amplitude of the transverse ac field caused by the current source (i.e. saturation). Also, a previous numerical investigation in Ref. [3] has found that when the external field is small, the effect of nonlinear coupling between the electromagnetic field and magnetization may not be negligible in studying the MI effect, as profound differences may be seen between the two approaches. In addition, experimental data presented for MI sensors has explored effects not considered explicitly in previous models, such as effects of temperature [4,5]. Also, an accurate understanding of the switching behavior in MI elements may be useful in material and sensor development. For example, research is active towards potential applications based on an understanding of double switching observed in magnetic alloys and/or magnetic multilayered structures as discussed in Ref. [6]. Additionally, the relationship between temperature and switching modes is relevant in other applications, for example, thermally assisted magnetization reversal [7]. Here, *switching mode* refers to the manner in which the magnetization field aligns itself with a driving ac external field over the volume of the MI element wire. The driving field is a transverse magnetic field due to the current source. The question arises as to whether all the magnetization

* Corresponding author.
E-mail address: kwaku_eason@dsi.a-star.edu.sg (K. Eason).

0304-8853/$ - see front matter © 2010 Elsevier B.V. All rights reserved.
doi:10.1016/j.jmmm.2009.12.023

changes in the MI element structure are simultaneous or do domain walls play a role in achieving the reorientation of all of the domains. For any small magnetic structure, the answer depends, in general, on sensor materials, geometry, and operating conditions. For example, it is well known that in very low input frequencies and at low field amplitudes, the switching mode can take place by way of reversible domain wall motion [8], in particular if equilibrium walls are present. But in larger uniform fields, additional switching modes can take place including irreversible domain wall motion as well as pure rotation. Additionally, when the frequencies are relatively high, the domain wall motion may be somewhat unfavorable due to the fact that moving domain walls have dynamic attributes. If the variation of the magnetic field is too fast and exceeds the amount of time required for the formation of a domain wall, then their formation and propagation become less favorable and this is referred to as domain wall damping. However, in MI sensors, a unique set of conditions are established where a non-uniform field at relatively high frequencies develops within the element and these conditions differ from the classical conditions upon which the above observations are typically based. Here, switching modes are examined under the conditions of the MI sensor. Relations to damping are also discussed here in the context of the MI sensor.

The influence of temperature on the magnetic permeability in magnetic alloys has been studied in the past. Historically, in measuring the effects of temperature on the magnetic permeability, two peaks have been observed experimentally [5,9,10]. One peak occurs near room temperature and a second peak may occur just before the Curie temperature. The second peak is referred to as the Hopkinson's peak (HP). This work discusses, strictly, the effects of temperature near room temperature and results discussed do not correlate to the HP, which has been explained on the basis of several mechanisms [11].

In the interest of investigating the MI effect using a more general approach suitable to examine dynamic switching modes in weak fields, one key assumption that is commonly made is relaxed here by solving a nonlinear coupled space–time numerical model for the cylindrical MI element structure to support a better understanding of the mechanisms driving the MI sensor. The higher-fidelity solutions so-obtained should offer a better prediction of MI device behavior and further insights to improved MI sensor designs.

The remainder of this paper then offers the following:

(1) An MI sensor analytical model is formulated preserving the coupling between the magnetic field, magnetization, and temperature; thus, it provides the ability to examine dynamic switching mode behavior under various conditions of interest, including temperature changes (near room temperature).
(2) The numerical model also deploys a meshless method (MLM) formulated in a point collocation formulation. A quasi-Newton nonlinear scheme is also used in an implicit integration algorithm to further enable computations on a desktop PC.
(3) The weak-field (nonlinear MI) regime is considered here by solving the problem in zero (H_e=0) external field under common MI configurations. This region is highly nonlinear and serves as a good representation of behavior in the weak field regime [3]. Also, the MI effect is studied here using experimentally reported conditions and parameters.

Using this approach, computations for important cases are discussed, one of which has received minimal consideration (effects of temperature). Also, most previous works have only considered contributions from axially distributed Neel domain walls in the MI sensor. Here, dynamic radial domain walls are considered, and it is shown that (radial) domain walls possibly play a very important role in the MI effect contributing to previously reported experimental observations including temperature and frequency effects.

2. MI effect analytical formulation

The following coupled nonlinear equations of motion, along with boundary conditions and initial conditions, describe the magnetic field intensity **H**, the magnetization **M**, the demagnetization potential φ_D, and the temperature T.

The space–time behavior of the magnetic field intensity **H**, described by classical electrodynamics, is given by the Maxwell's equation in the form

$$\frac{\partial \mathbf{B}}{\partial t} = -\frac{1}{\sigma(T)}(\nabla \times \nabla \times \mathbf{H}) \tag{1}$$

where, the magnetic flux density $\mathbf{B}=\mu_0\mathbf{H}+\mathbf{M}$, where μ_o is the magnetic permeability in free space; and $\sigma(T)$ is the bulk electrical conductivity, depending on the local temperature T.

The magnetization "motion" is governed by a norm-preserving micromagnetics equation where the Gilbert form is used given by

$$\frac{\partial \mathbf{M}}{\partial t} = -\gamma \mathbf{M} \times \mathbf{H}_T + \frac{\alpha}{M_s(T)}\mathbf{M} \times \frac{\partial \mathbf{M}}{\partial t} \tag{2}$$

In (2), γ is the gyromagnetic ratio given here by $\mu_0 q_e/m_e$ [12] where q_e is the electron charge and m_e is the electron mass; α is the dimensionless phenomenological Gilbert damping constant; and $M_s(T)$ is the temperature dependent saturation magnetization. In (2), it is understood that at each point in space and time $||\mathbf{M}||=M_s(T)$. In addition, $\mathbf{H}_T$ is the total effective field given by

$$\mathbf{H}_T = \mathbf{H} + \mathbf{H}_K + \mathbf{H}_X + \mathbf{H}_D \tag{2a}$$

where **H** is the external field described by (1); $\mathbf{H}_K$, $\mathbf{H}_X$ and $\mathbf{H}_D$ are the effective fields taking into account the effects of anisotropy, exchange, and demagnetization, respectively. We also note that due to MI elements having low magnetostriction, magnetoelastic contributions are ignored.

The uniaxial anisotropy field $\mathbf{H}_K$ is given by

$$\mathbf{H}_K = (H_K/M_s)(\mathbf{M}\cdot\mathbf{e}_k)\mathbf{e}_k \tag{2b}$$

In (2a), $H_K(T)=|\mathbf{H}_K|=2K(T)/M_s(T)$ where $K(T)$ is the first anisotropy constant; and $\mathbf{e}_k$ is the unit vector in the direction of the material preferred anisotropy. The exchange field $\mathbf{H}_X$ is given by

$$\mathbf{H}_X = A_X \nabla^2 \mathbf{M} \tag{2c}$$

where A_X is the exchange stiffness (scalar).

The long range interior demagnetization field $\mathbf{H}_D$ is characterized here by the Poisson equation

$$\mu_0 \nabla^2 \varphi_D = \nabla \cdot \mathbf{M} \tag{3}$$

where

$$\mathbf{H}_D = -\nabla \varphi_D \tag{3a}$$

The thermal diffusion equation describing the temperature T within the MI element is given by

$$\rho c_p(T)\frac{\partial T}{\partial t} = \frac{\partial k}{\partial T}||\nabla T||^2 + k(T)\nabla^2 T + \frac{1}{\sigma(T)}||\nabla \times \mathbf{H}||^2 \tag{4}$$

where ρ is the mass density of the wire; c_p is the specific heat capacity; and k is the thermal conductivity.

The switching mechanism can be investigated by numerically solving (1)–(4). To solve these four coupled nonlinear equations for **H**, **M**, φ_D, and T with variations in both space and time (r, t) [13], relevant boundary (BC) and initial conditions are also

required and are specified in Sections 2.1 and 2.2, respectively. The parameters that depend on temperature here include $\sigma(T)$, $k(T)$, $M_s(T)$, K(T), and $c_p(T)$. The treatment of the temperature dependent parameters used here is discussed in Section 2.3. The amorphous magnetic alloy $Co_{68.15}Fe_{4.35}Si_{12.5}B_{15}$ has been chosen here because a partial validation can be made against experimentally reported data from Ref. [17].

2.1. Boundary conditions

The model describes the radial variation as a function of time t. For the given problem, the normal component of **B** is zero on the surface, which leads to the following equation for H_r:

$$\mu_0 H_r + M_r = 0 \tag{5}$$

The BCs along the centerline of the circular wire are given by

$$r = 0 \quad \partial H_z/\partial r = H_\theta = M_{r,\theta} = \partial M_z/\partial r = \varphi_D = \partial T/\partial r = 0 \tag{6}$$

For the transverse (circular) component, the use of a current source in a material surrounded by air allows the BC to be simplified to requiring only the medium of the MI element, and allows ignorance of any nonconductive surrounding medium. This follows from integrating Ampere's law to arrive at an explicit Dirichlet BC for H_θ. With this, the MI element BCs for **H**, **M**, φ_D, and T on the surface are given by

$$r = r_0 \quad H_\theta|_{r=r_0} = I_s(t)/2\pi r_0; \;\; H_z|_{r=r_0} = H_e \tag{7a, b}$$

$$\frac{\partial \mathbf{M}}{\partial n}|_{r=r_0} = 0 \tag{7c}$$

$$(-\mu_0 \nabla \varphi_D + \mathbf{M})|_{\partial\Omega} \cdot \mathbf{n} = 0 \tag{7d}$$

$$-k \nabla T|_{\partial\Omega} \cdot \mathbf{n} = h(T|_{\partial\Omega} - T_\infty) \tag{7e}$$

In Eq. (7c), where **n** is the unit vector along the radial direction, assumes the free spinning condition, i.e. no localized torques on the surface [14]. In (7e), h is the thermal convection coefficient; and T_∞ is the temperature of the surrounding environment.

2.2. Initial condition

The IC is assumed uniform at t=0. The magnetization is assumed oriented along the axis (z-axis) of the wire, parallel to $\mathbf{e}_K$, leading to

$$\mathbf{H}(r,0) = \varphi_D(r,0) = 0 \tag{8a}$$

$$\mathbf{M}(r,0) = \begin{bmatrix} 0 & 0 & M_s \end{bmatrix}^T \tag{8b}$$

$$T(r,0) = T_\infty \tag{8c}$$

2.3. Temperature dependence of parameters

For the temperature range considered, the experimental material $Co_{68.15}Fe_{4.35}Si_{12.5}B_{15}$ has not had these material properties measured and/or sufficiently reported, and thus their values are necessarily estimated here. In many cases, however, a single data point (at room temperature) has been measured, and so the temperature dependence of the parameters is approximated using commonly observed characteristic curves that pass through these reported single data points for the material. A summary of the relations used is given next.

2.3.1. Electrical conductivity

The bulk resistivity ($1/\sigma$) is approximated as a second order parabolic temperature dependence. The relation, which has been designed to pass through the data point reported in [15] for the material considered, is given by

$$\rho(T) = 1/\sigma(T) \approx \rho_0 + CT^2 \tag{9}$$

2.3.2. Thermal conductivity

The thermal conductivity $k(T)$ was approximated by computing the volume compositional average for $Co_{68.15}Fe_{4.35}Si_{12.5}B_{15}$ using reported values for the constituent materials over the temperature range considered [16].

2.3.3. Saturation magnetization

The saturation magnetization dependence on temperature in magnetic alloys has been studied in the past; the specific relation used here has been discussed in Ref. [17], where the saturation magnetization in the alloy is approximated by

$$M_s(T) = M_{s0}(1 - T/T_c)^\beta \tag{10}$$

where M_{s0} is the value at T=0; T_c is the Curie temperature; the value for β has been reported from experimental measurements in both iron and cobalt where β=0.36 [17]. T_c has also been reported for this material, T_c=310 °C [18].

2.3.4. Anisotropy constant

The variation of the first anisotropy constant with temperature has been approximated using a hyperbolic tangent function, inspired by classical curves reported for cobalt and iron [8]. The curve used here has been scaled to be consistent with the *as cast* data point for the considered material reported in [19], and subsequently estimated after annealing. The relation is given by

$$K(T) = -K_0 \tan h(\varsigma(T - T_0)) + K_m \tag{11}$$

The parameter ζ controls the variation rate with temperature and has also been estimated based on previously reported values of $K(T)$ for cobalt and iron [8].

2.3.5. Specific heat capacity

Similar to the thermal conductivity, $c_p(T)$ is approximated by computing the volume compositional average (with cobalt and iron) using reported values over the temperature range considered [16].

3. Numerical simulations and discussion

The equations of motion form a coupled nonlinear system with variations in both space and time (r, t) [13]. Using Eqs. (1)–(7), the cylindrical MI sensor element is spatially discretized using a point collocation (PC) formulation using meshless methods (MLM) [20]. In the PC-MLM formulation, the *Hp*-Cloud MLM shape functions using discontinuous weighting functions are deployed to avoid some known stability issues near the boundaries in MLM-PC formulations, which have been discussed in previous works [21]. The MLM formulation is summarized in the Appendix. The time integration is done here using a second order implicit Newmark integration scheme along with projection of the magnetization vector to stabilize the algorithm [22]. At each time step, a nonlinear equation is solved and a quasi-Newton solver is used known as Broyden's method [23].

Table 1 tabulates the values of the temperature dependent parameters used in the simulations which are computed for a circular amorphous magnetic alloy ($Co_{68.15}Fe_{4.35}Si_{12.5}B_{15}$) [17] wire of radius 15 μm and length 5 mm. Other values of the material parameters used here are summarized in Table 2.

In the simulations discussed here, the wire assumes a uniform axial anisotropy axis $\mathbf{e}_K$, although there is evidence of a non-uniform anisotropy orientation along the radius of the wire [19]. Another relevant point is that 180° transverse Neel walls have

also been observed along the axis of the wire. Given this equilibrium configuration, the choice of an axial anisotropy represents the center of the Neel wall, where the equilibrium magnetization points along the wire axis. This location also represents a potential location for nucleation of longitudinal wall motion (with respect to an ac transverse field), due to a lower energy requirement to switch (only needs a 90° turn *vs.* 180°).

Solutions for 2.5 current cycles have been computed and stable behavior is established in the second cycle at the latest. Thus, data from the second and third cycles are primarily used in the discussions that follow.

Computed results have been obtained for three specific behaviors of the MI effect; the switching mode, temperature and frequency. First, the switching mode predicted by the coupled nonlinear space–time model is discussed. This is required to explain the predicted effects of temperature and frequency on the MI effect. Additionally, computed results are compared (for partial validation) against previously publish experimental data in the discussion of frequency effects.

3.1. Magnetization switching mode

Fig. 1 shows six "snapshots" of the magnetization spatial profile in a cycle for a cylindrical quarter illustrating the switching mode in the MI element considered. The results reveal that for conditions taken from realistic MI sensors materials, as given in Table 2 (at 1 MHz), a dynamic domain wall motion nucleating at the surface achieves the switching. Unlike an equilibrium domain wall that typically forms semi-permanently in self-minimizing the energy of the magnetic structure in the absence of time varying external fields, the formation of this dynamic wall is in the presence of a very active and nonuniform dynamic external field H_θ. The dynamic domain wall develops on the surface, where the field is maximum, and propagates into the core until the wire is homogeneously transverse in one direction.

It has been previously mentioned in some works that in this type of MI element at 1 MHz, Neel domain wall motion [24]. However, for the case of the radial domain walls, a more general coupled nonlinear model used here reveals that the structure switches by developing propagating radial domain walls even at 1 MHz whose apparent length scale easily "fits" into the wire. The observation of the domain wall length scale is discussed in more detail in a forthcoming work. Thus, the results here suggest that the role of domain wall dynamics, including radial walls, in the MI effect may be much more significant than originally believed for the frequencies considered.

Estimates of the domain wall velocity in Fig. 1 is approximately 20 m/s (or 45 mi/hr). The domain wall motion is also seen to have non-uniform velocity, starting from $v_{dw}=0$ at the surface, then increasing in the core, and later decreasing as the wall gets closer to the center.

Table 1
Temperature dependent parameters.

T (K)	300	400	500
σ $(\mu\Omega\,\mathrm{m})^{-1}$	0.769	0.500	0.345
k (kW/m K)	74.23	61.22	54.77
c_p (kJ/kg K)	301.49	327.99	347.88
M_s (T)	0.8101	0.6926	0.5212
K (J/m^3)	0.1912	0.1547	0.1148

Table 2
Additional simulation parameters.

f (MHz)	I_s (mA)	h (kJ m^{-2} K^{-1})	α	A_X (J/m^2)
1–1000	15	200	0.01	10^{-11}

3.2. Effects of elevated temperature

The MI effect model has been used to examine the initial increase in the MI voltage starting from room temperature (300 K) well before approaching the expected decrease as T approaches the Curie temperature [5]. The results are presented in Figs. 2 and 3, where the MI effect (for $f=1$ MHz) is simulated at ambient environmental temperatures of $T_\infty=27$ °C (300 K), 77° (350 K), and 127 °C (400 K).

Figs. 2(a) and (b) plot the radial distributions of the transverse magnetic field intensity $H_\theta(r,t_p)$, and the corresponding magnetization distributions $M_\theta(r,t_p)$ in the wire at the three distinct temperatures. The point in time is taken at the second ac current peak time t_p in the second cycle of calculations (i.e. $\omega t_p=5\pi/2$).

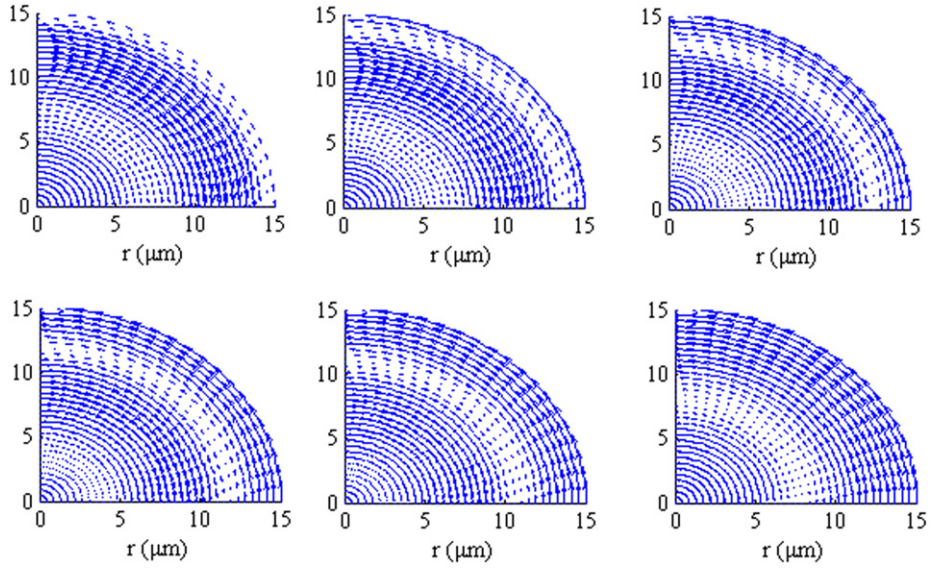

Fig. 1. Illustration of the radial domain wall in switching of circular MI sensor for 15 μm radius wire, $f=1$ MHz, at $T=300.10$ K.

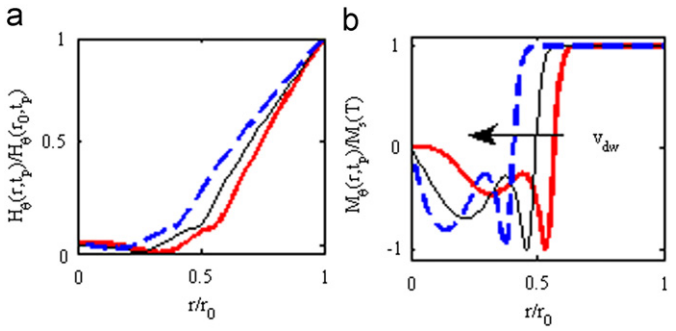

Fig. 2. H_θ and M_θ spatial profiles for T_∞=27, 77, and 127 °C. Dashed leftmost curves ⇒27 °C, rightmost solid curve = > 127 °C

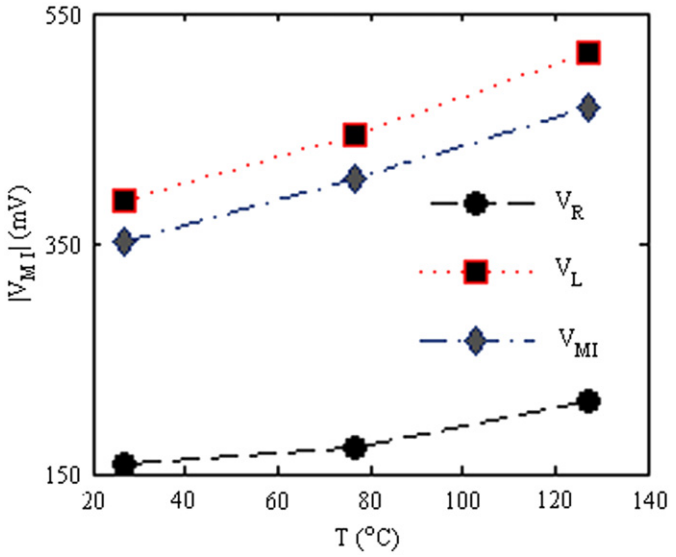

Fig. 3. MI voltage components (ohmic, inductive, total) at T_∞=27, 77, 127 °C.

Each field intensity $H_\theta(r,t_p)$ is normalized by the peak value at the surface, $H_\theta(r_0,t_p)=|I_s|/2\pi r_0$, while the magnetization is normalized by $M_s(T)$ for each temperature given in Table 1. Fig. 3 shows the amplitude components of the MI voltage V_{MI} as a function of temperature

$$V_{MI}(t)=V_R(t)+V_L(t) \tag{12}$$

where

$$V_R(t)=\frac{L}{\pi\sigma(T)r_0^2}I_s(t) \quad \text{and} \quad V_L(t)=-\frac{d\Phi(t)}{dt} \tag{12a, b}$$

It is noted that (12a) is typically considered to be appropriate in low frequencies, however, results from the model used here show that the current is distributed (although non-uniformly) throughout nearly all of the wire at 1 MHz (i.e. a weak skin effect is observed), and thus (12a) is still used as an approximation for the case of a weak skin effect. However, above 1 MHz, a strong skin effect develops and thus (12a) is much more inappropriate and the changes in ohmic losses are estimated at these higher frequencies by computing a modified dc resistance using the actual penetrated area of the current instead of the whole wire cross-section. This modification is used in Section 3.3 in the discussion of frequency effects. With this, some observations from Figs. 2 and 3 are discussed as follows:

- As shown in Fig. 2(a), although a weak skin effect is observed, the distribution of the magnetic field intensity H_θ within the wire is "widened" as the temperature is elevated above room temperature. This can be explained by Maxwell's Eq. (1) for the magnetic field H_θ as follows: The ac current in the MI element introduces a skin effect (weak in this case) [26] in the field, where an approximate length of distribution (from the surface inward) is given by

$$\delta_s \propto 1/\sqrt{\sigma(T)\mu_\theta\omega} \tag{13}$$

Eq. (13) reveals that the distribution widening in H_θ is a result of the reduction in the electrical conductivity $\sigma(T)$ as temperature increases.

- Fig. 2(b), which shows the progress of the moving domain wall at the same point in time for the three temperatures, further suggests that the dynamic domain wall propagates at a higher average speed v_{dw} from the surface towards the center at elevated (above room) temperature. Even for seemingly small changes in H_θ. This observation is reasonable based on the well known characteristic of domain walls that they can be moved with very small magnetic field intensities.
- The increase in the inductive voltage V_L with temperature shown in Fig. 3 can then be explained by the resulting micro-scale domain wall dynamics. To illustrate this Fig. 4 shows a simple schematic of the switching domain wall motion near the surface of the wire as predicted by the model used here. In the circular wire, because of geometrical factors and $H_\theta(r=0)=0$, the transverse magnetization is also negligible at the center for the circular wire. Thus, $M(r=0)\approx 0$, leading to the simple illustrative diagram shown below (also see Fig. 2b). Fig. 4 shows that the change in flux is given by the difference between the area under Profiles 1 and 2. Thus, the shaded area in Fig. 4 represents the change in flux. It follows that the inductive voltage can be approximated from (12a) as follows:

$$V_L \propto L_z \frac{d}{dt}\int_0^{r_0} M_\theta\, dr \approx L_z M_s(T)\frac{\Delta r}{\Delta t} \tag{14}$$

From Fig. 2(b), an increase in the dynamic domain wall velocity ($v_{dw}=\Delta r/\Delta t$), due to the higher magnetic field gives rise to an increased voltage based on (14). However, (14) also suggests that eventually the effects of a decreasing $M_s(T)$ and likely other parameters such as anisotropy $K(T)$ begin to dominate causing the expected eventual decline of the MI voltage with temperature.

3.3. Effects of frequency on the MI effect

One of the objectives in this section is to validate the coupled micromagnetic model formulation used here. Fig. 5 shows the

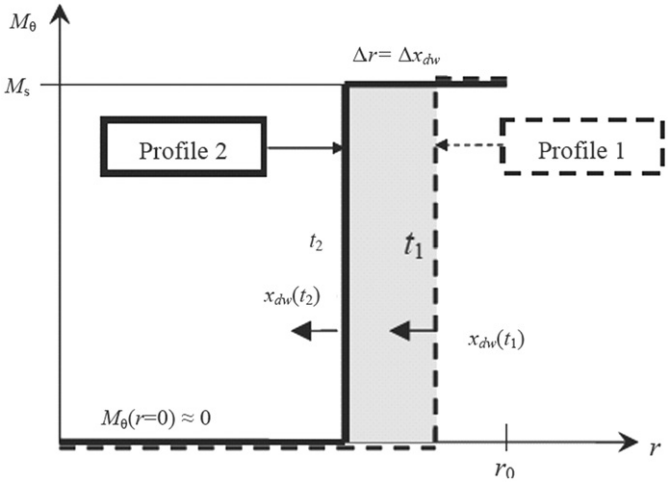

Fig. 4. Simplified MI element domain wall motion and illustration of domain wall velocity in relation to M_θ profiles.

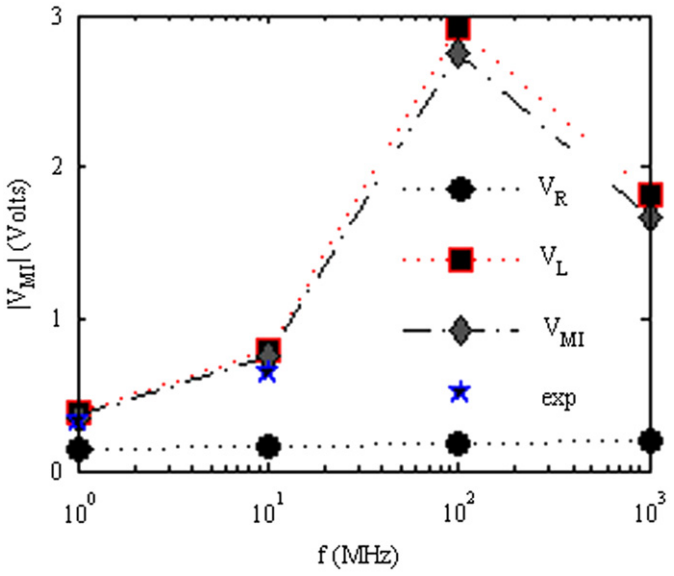

Fig. 5. $|V_{MI}|$ components (ohmic, inductive, total) , compared to experiment [ ], with fequency f from 1 MHz to 1 GHz.

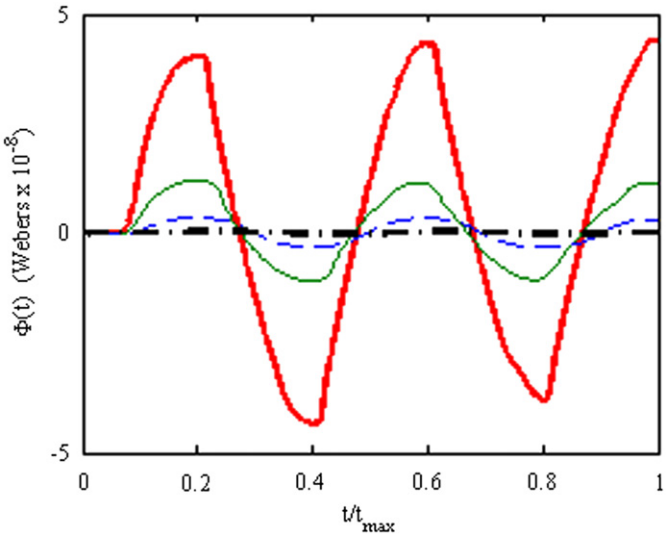

Fig. 6. Magnetic flux used in (12b) with time *vs.* frequency f. Largest amplitude (solid curve) $\Rightarrow$ 1 MHz, smallest amplitude (dashed curve) $\Rightarrow$ 1000 MHz.

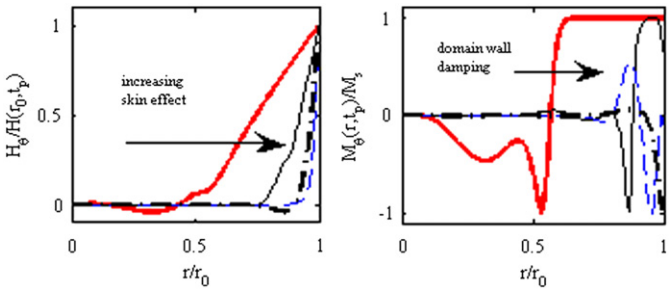

Fig. 7. Variations of H_θ and M_θ with all four different frequencies f=1, 10, 100, and 1000 MHz. Solid leftmost curves $\Rightarrow$ 1 MHz, rightmost dashed curve $\Rightarrow$ 1000 MHz.

voltage components with frequency, where the evaluation of the errors (in %) is based on differences relative to reported experimental data [15] as follows:

$$e_x = \frac{V_{MI} - V_{MI}(\text{exp})}{V_{MI}(\text{exp})}$$

The results are computed at four different operating frequencies (1, 10, 100, and 1000 MHz). For the two available published data points at 1 and 10 MHz, the coupled nonlinear analytical space–time model agrees reasonably well (within 8% and 17% differences, respectively). Note that this order of error represents a significant improvement for the nonlinear regime, where much larger errors have been highlighted in this region for decoupled MI sensor models as high as 100 s of percent [3]. As shown in Fig. 5, V_{MI} increases with frequency up to a certain frequency then decreases. This behavior is known and has already been demonstrated experimentally in MI sensors in Ref. [27]. In Fig. 6, the harmonic flux at each frequency is computed by

$$\Phi(t) = \int_S [\mu_0 H_\theta(t) + M_\theta(t)] d\mathbf{s} \tag{15}$$

where S is the flux integrating area in the (r, z) plane.

Results here illustrate that the micro- and macro-behavior are closely coupled in the MI sensor where the distribution of the field link closely to domain wall dynamics, etc. To explain the coupling effect of the micro-scale domain wall dynamics on V_{MI}, Figs. 7(a) and (b) graph the corresponding $H_\theta(r,t_p)$ and $M_\theta(r,t_p)$ profiles for the four frequencies. The following observations made in Figs. 5 and 7 explain the effects of micro-scale domain wall dynamics on V_{MI} with frequency:

- As the frequency changes, a flux change (with f) is due to the evolving skin effect caused by the ac current source. Fig. 6 shows that as f increases, the flux amplitudes decrease due to this effect. However, in the case of increased (low) frequency, the increasing rates for H_θ cause faster domain walls by turning the magnetic moments faster, which increases the inductive voltage in the wire as discussed in Section 3.2, even though the flux amplitudes are decreasing.
- However, at ultrahigh frequencies, V_{MI} decreases with f, on the order of 100 MHz to 1 GHz as shown in Fig. 5, which is consistent with experiments in similar wires [26]. A factor contributing to the decrease in V_{MI} is given as follows: As the frequency increases, the H_θ profile becomes increasingly confined to the surface due to the skin effect as shown in Fig. 7(a). At very high frequencies, these developing conditions are not conducive to both form and propagate a domain wall towards the center and complete switching of the whole wire. The domain wall travels less and less into the wire resulting in a vanishing inductive voltage by way of both a lack of a driving force into the wire and dynamic domain wall damping ensues as the variation of the source becomes too fast. The result is that V_{MI} begins to diminish with frequency.

4. Conclusion

In this work, we have numerically solved a coupled nonlinear space–time model to investigate MI effects under dynamic conditions that have been reported in the literature. Here, a weak-field behavior has been considered (H_e=0), specifically, where coupling is more important. The model has also been enabled by use of a spatial discretization tool known as meshless methods formulated in a point collocation scheme. This approach has enabled the study of the MI effect under the influence of both temperature and frequency. The predicted switching mode and its behavior by way of dynamic domain walls has been shown to explain experimental observations reported elsewhere, where elevated temperature near room temperature speeds up domain walls causing an increased voltage (temporarily). Also, the decline

in MI voltages at ultrahigh frequencies has been shown to be due to dynamic domain wall damping because of a receding penetration of the wall into the MI element.

Acknowledgment

This work has been supported, in part, by a graduate fellowship through the US Office of Naval Research.

Appendix. *Hp*-Cloud MLM shape functions in MLM

Given $\mathbf{H}(\mathbf{x},t)$, $\mathbf{M}(\mathbf{x},t)$, $\varphi_D(\mathbf{x},t)$, and $T(\mathbf{x},t)$, each component, for example, of the vector unknown $\mathbf{H}$ is an independent scalar degree of freedom, u. To derive the MLM shape functions used here, which are not closed form functions, each degree of freedom, u, begins with a definition given by

$$u_i(x) \cong u^{\rho}(x, x_k; \rho) = \sum_{j=1}^{p} \varphi_j a_j = \varphi_v A \tag{A1}$$

$\mathbf{x}$ and $\mathbf{x}_k$ are global (from anywhere in the domain) and local (only near $\mathbf{x}$) positions, respectively, within the computational domain. The basis function coefficients, a_j (which are unknown) are associated with each independent basis function, φ_j and are often taken from the set of monomials that span the set of polynomials in $\mathbf{R}^n$. For example, the one dimensional basis functions, φ_j, for a 3nd order *reproducible* formulation, are given by

$$\{\varphi\} = \{1, x, x^2, x^3\} \tag{A2}$$

Then, to determine the coefficients A uniquely, in the case of the *Hp*-Cloud formulation used here [28], a discrete moving least square problem is solved. A localized discrete cost function, $\mathbf{J}_d$, is defined by

$$J_d = \sum_{k=1}^{n} w\left(\frac{x-x_k}{\rho}\right)\left(u_k - \sum_{j=1}^{p} \varphi_j\left(\frac{x-x_k}{\rho}\right) a_j\right)^2 \tag{A3}$$

The weighting function, w, is chosen to provide compact support. n is the number of local support nodes. Minimizing (A3) to solve for parameters a_j results in the following equations:

$$\mathbf{TU} = \mathbf{M}_m A \Rightarrow A = \mathbf{M}_m{}^{-1}\mathbf{TU} \tag{A4}$$

The final shape functions can be computed as

$$u(\mathrm{x}) \cong \varphi_v \mathbf{M}_m{}^{-1}\mathbf{TU} = \Psi_v^s \mathbf{U} \tag{A5}$$

$\mathbf{M}_m$ is a $p \times p$ matrix, often referred to as a moment matrix, and p is the number of monomial basis functions, e.g. in (A2) p=4, whose matrix elements are given by

$$M_{m,ij} = \sum_{k=1}^{n} \varphi_i\left(\frac{x-x_k}{\rho}\right) w\left(\frac{x-x_k}{\rho}\right) \varphi_j\left(\frac{x-x_k}{\rho}\right) \tag{A6}$$

$\mathbf{T}$ is a $p \times n$ matrix, whose elements are given by

$$T_{ij} = w\left(\frac{x-x_j}{\rho}\right) \cdot \varphi_i\left(\frac{x-x_j}{\rho}\right) \tag{A7}$$

The result is an approximation of the degree of freedom u in terms of the final shape functions given by

$$u^{\rho}(x) = \sum_{j=1}^{n} \Psi_j^S u_j \tag{A8}$$

Ψ_j^S are the final *Hp*-Cloud MLM shape functions. The approximation in (A8) is then used explicitly in a point collocation scheme to define each degree of freedom, where, for the MI effect variables, we have

$$\begin{aligned} \mathbf{H}(x) &\cong \sum_{j=1}^{n} \Psi_j^s \mathbf{H}_j, \mathbf{M}(x) \cong \sum_{j=1}^{n} \Psi_j^s \mathbf{M}_j \\ \varphi_{\mathrm{D}}(x) &\cong \sum_{j=1}^{n} \Psi_j^s \varphi_{Dj} T(x) \cong \sum_{j=1}^{n} \Psi_j^s T_j \end{aligned} \tag{A9}$$

References

[1] O.V. Lounasmaa, H. Seppa, SQUIDs in neuro- and cardiomagnetism, Journal of Low Temperature Physics 135 (2004) 295–335.
[2] K. Mohri, T. Uchiyama, L.V. Panina, Recent advances of micro magnetic sensors and sensing application, Sensors and Actuators A: Physical 59 (1997) 1–8.
[3] K. Eason, K.M. Lee, Effects of nonlinear micromagnetic coupling on the weak-field magneto-impedance sensors, IEEE Transactions on Magnetics 44 (2008) 2042–2048.
[4] A.A. Rakhmanov, N. Perov, P. Sheverdyaeva, A. Granovsky, A.S. Antonov, The temperature dependence of the magneto-impedance effect in the Co-based amorphous wires, Sensors and Actuators A: Physical 106 (2003) 240–242.
[5] H. Chiriac, C.S. Marinescu, T.A. Ovari, Temperature dependence of the magneto-impedance effect, Journal of Magnetism and Magnetic Materials 196 (1999) 162–163.
[6] M.A.I. Nahid, T. Suzuki, Double switching hysteresis loop in a single layer Fe3Pt alloy thin films,, Thin Solid Films 516 (2008) 2063–2066.
[7] Y. Nozaki, B. Purnama, K. Matsuyama, Micromagnetic simulation of thermally assisted magnetization reversal in magnetic nanodots with perpendicular anisotropy, Journal of Magnetism and Magnetic Materials 310 (2007) 2683–2685.
[8] C. Kittel, Physical theory of ferromagnetic domains, Reviews of Modern Physics 21 (1949) 541–583.
[9] O. Popov, M. Mikhov, Hopkinson effect in an assembly of single domain particles-thermomagnetic curves of Nd2Fe14B-type ribbons, Journal of Magnetism and Magnetic Materials 75 (1988) 135–140.
[10] H. Pfeiffer, W. Schuppel, Temperature dependence of the magnetization in fine particle systems and the Hopkinson effect. Application to barium ferrite powders, Journal of Magnetism and Magnetic Materials 130 (1994) 92–98.
[11] G. Bordin, G. Buttino, A. Cecchetti, M. Poppi, Temperature dependence of magnetic properties of a Co-based alloy in amorphous and nanostructured phase,, Journal of Magnetism and Magnetic Materials 195 (1999) 583–587.
[12] B. Hillebrands, K. Ounadjela, Spin Dynamics in Confined Magnetic Structures II (Topics in Applied Physics-87), 2003.
[13] A. Prohl, Computational Micromagnetism: Teubner, 2001.
[14] G.T. Rado, J.R. Weertman, Spin-wave resonance in a ferromagnetic metal, Journal of the Physics and Chemistry of Solids 11 (1959) 315–333.
[15] K. Mohri, K. Bushida, M. Noda, H. Yoshida, L.V. Panina, T. Uchiyama, Magneto-impedance element, IEEE Transactions on Magnetics 31 (1995) 2455–2460.
[16] F.P. Incropera, D.P. DeWitt, in: Fundamentals of Heat and Mass Transfer, John Wiley & Sons, 1996.
[17] G. Herzer, Grain structure and magnetism of nanocrystalline ferromagnets, IEEE Transactions on Magnetics 25 (1989) 3327–3329.
[18] H. Chiriac, C.S. Marinescu, T.-A. Ovari, Temperature dependence of the magneto-impedance effect in Co-rich amorphous glass-covered wires,, Journal of Magnetism and Magnetic Materials 215 (2000) 539–541.
[19] K. Mohri, F.B. Humphrey, K. Kawashima, K. Kimura, M. Mizutani, Large Barkhausen and Matteucci effects in FeCoSiB, FeCrSiB, and FeNiSiB amorphous wires, IEEE Transactions on Magnetics 26 (1990) 1789–1791.
[20] G.R. Liu, in: Mesh free methods: moving beyond the finite element method, CRC Press, 2003.
[21] K.-M. Lee, Q. Li, H. Sun, Effects of numerical formulation on magnetic field computation using meshless methods, IEEE Transactions on Magnetics 42 (2006) 2164–2171.
[22] L.U. Banas, Numerical methods for the Landau–Lifshitz–Gilbert equation, Rousse, Bulgaria, 2005.
[23] R.L. Burden, J.D. Faires, in: Numerical Analysis, PWS Publishing Company, 1993.
[24] D. Atkinson, P.T. Squire, Phenonemological model for magnetoimpedance in soft ferromagnets, Journal of Applied Physics 83 (1998) 6569.
[26] J.D. Jackson, Classical Electrodynamics: Wiley & Sons, Inc, 1999.
[27] D. Menard, M. Britel, P. Ciureanu, A. Yelon, Giant magnetoimpedance in a cylindrical magnetic conductor, Journal of Applied Physics 84 (1998) 2805–2814.
[28] C.A.M. Duarte and J.T. Oden, HP Clouds—A Meshless Method to Solve Boundary-Value Problems, University of Texas at Austin, Technical Report 95–105 1995.